ACS Catalysis

Research Article

pubs.acs.org/acscatalysis

Ordered Hierarchically Micro- and Mesoporous Fe−N_x-Embedded Graphitic Architectures as Efficient Electrocatalysts for Oxygen Reduction Reaction

Aiguo Kong, Xiaofang Zhu, Zhen Han, Youyi Yu, Yongbo Zhang, Bin Dong, and Yongkui Shan*

Department of Chemistry, East China Normal University, 500 Dongchuan Road, Shanghai 200241, P. R. China

Supporting Information

ABSTRACT: A series of novel ordered hierarchically micro- and mesoporous Fe−N_x-embedded graphitic architectures (Fe−N−GC) are directly prepared by the simple pyrolysis of the different nitrogen heterocyclic compounds and iron chlorides in the confined mesochannels of SBA-15. Among these porous Fe−N−GC materials, the sample prepared by heating 2,2-bipyridine and Fe chelates at 900 °C shows the more positive ORR onset potential and half-wave potential (E 1/2) values than commercial Pt−C catalysts in 0.1 M KOH, which illustrate that it is one of the most-promising nonprecious metal catalysts (NPMCs) among the reported NMPCs in alkaline medium. Moreover, unlike nitrogen-doped carbons and Co_3O_4/carbon composites, high ORR current density (5.2 mA cm^{-2}, 0.6 V) over this Fe−N−GC electrode with catalyst loading of 0.6 mg cm^{-2} can be also obtained in 0.1 M $HClO_4$ acidic solution, which is about 0.6 mA cm^{-2} larger than that over the electrode of commercial Pt/C with 20 μg_{Pt} cm^{-2} loading. In addition, the effective embedding of active moieties in the graphitic frameworks and a direct four-electron reduction pathway in ORR contributes to its high durability in both alkaline and acidic media. Its excellent ORR activity should be ascribed to the optimized balance between active site density and capability for mass and charge transport. Such hierarchically porous Fe−N_x−graphitic materials hold great promise for the practical utilization in cathode catalyst layers of proton exchange membrane fuel cells.

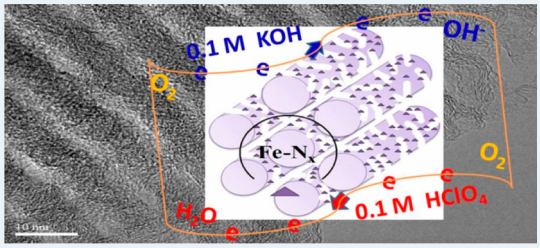

KEYWORDS: *hierarchically porous structures, direct synthesis, nanostructures, oxygen reduction, nonprecious metal catalysts*

INTRODUCTION

The increasing efforts are directed toward exploring the efficient nonprecious metal catalysts (NPMCs) to replace the expensive Pt-based catalysts for bringing the energy techniques such as Li−O_2 batteries and proton exchange membrane fuel cells (PEMFCs) into real applications.[1] Transition metal−nitrogen-carbon (M−N−C) materials, especially for Fe−N−C,[2] were demonstrated as the practically most promising NMPCs for oxygen reduction reaction (ORR), owing to their high catalytic activity in wide pH ranges. However, a single active site of M−N−C often has the poor intrinsic ORR catalytic activity (TOF = 0.4 s^{-1}) compared to Pt (TOF = 25 s^{-1}).[3] For obtaining nonprecious metal electrodes with sufficient catalytic activity for ORR, active sites density in M−N−C catalysts must be effectively increased.[1c] In this regard, the most desirable M−N−C materials should possess high accessible surface area, plenty of active sites embedded in the graphitic carbon matrixes, facile reactant and product transport through a thick catalyst layer,[4] and eminent electron conductivity, which strongly depend on the pore structure and graphitization-degree of M−N−C catalysts, as well as the type of nitrogen and transition-metal precursors used.[1e,2b,5]

In order to have these functions available, special attention has been given to fabrication of the porous M−N−C catalysts with different morphologies.[3b,6] For example, ORR activity for Fe−N−C catalysts obtained by heating porous carbon-supported Fe phenanthroline complexes can be significantly enhanced. The ORR activity of catalyst obtained from the porous "Black Pearls" carbon with surface area of 1500 m^2 g^{-1} is about 1 order of magnitude higher than that of the catalyst obtained from the porous "Vulcan XC72" carbon with surface area of 254 m^2 g^{-1}.[7] Fe-based catalysts prepared by a ball-milling method that fill the pores of microporous carbon support with pore filler and Fe precursors followed by calcinating first in argon, then in ammonia, show a factor of >35 activity enhancement relative to the highest activity over the previous Fe-based catalysts in the literature.[3b,7] However, in these porous M−N−C catalysts reported, the porous materials mostly play a role of the support[8] or a platform for creating the catalytic active sites.[9] Only a few of M−N−C materials possess the porosity in themselves and are directly used as the catalysts for ORR.[1c] The porous M−N−C materials were generally prepared by the template-assisted synthesis route, for which onset potentials up to 0.85 V (vs RHE) and hydrogen peroxide production below 10% were often observed during the ORR.[10] The spectacular advancement in the ORR activity of M−N−C

Received: December 30, 2013
Revised: April 20, 2014
Published: April 23, 2014

   dx.doi.org/10.1021/cs401257j | ACS Catal. 2014, 4, 1793−1800

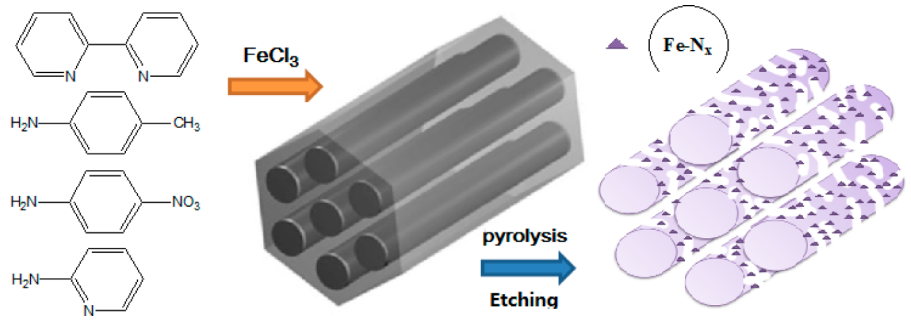

Figure 1. Synthesis of ordered hierarchically micro- and mesoporous Fe−N−GC materials.

catalysts notwithstanding, a large-scale commercialization of these M−N−C catalysts continues to face various challenges, such as a lack of M−N−C catalysts that combine enough ORR activity with good performance stability for the possible applications and the technical issues associated with the mass production of catalysts. At the same time, the cost of producing M−N−C catalysts and the corresponding fuel cell assembly is also a formidable impediment to their commercialization.

According to experimental facts mentioned above and theoretic analysis, it is well-known that the low active site density in catalysts may be compensated by increasing efficient electrode thicker in fuel cell, but the efficient thickness of electrode is limited due to mass- and charge-transport limitations in the catalysts. Thus, it should be acceptable that constructing the M−N−C materials with high active site density and strong capability for mass- and charge-transport will be a reasonable route that can remarkably upgrade the catalytic performance of this kind of catalyst. On the basis of the above consideration, we initiate a research effort to develop graphitic M−N−C catalysts having a combination of microporosity and mesoporosity properties that simultaneously maximizes active site density, oxygen transport, and electron conduction. Ordered hierarchically porous Fe−N_x-embedded graphitic architectures (Fe−N−GC) with appropriate accessible surface area are successfully prepared by the direct pyrolysis of simple and inexpensive nitrogen heterocyclic compounds and Fe salts in confined mesochannels of SBA-15. The advantage of this preparation method (shown in Figure 1) is an in situ-formed carbon matrix with a homogeneous distribution of catalytically active centers on the complete surface (involving pore wall), and the prepared materials show the excellent catalytic activity toward ORR in both alkaline and acidic media.

EXPERIMENTAL SECTION

Synthesis of Fe−N−GC Materials. Ordered mesoporous Fe−N−GC materials were prepared through the nanocasting synthesis procedures including filling of precursors, pyrolysis, and etching of templates. In a typical synthesis, 0.6 g of dried SBA-15[11] was added into a 20 mL alcohol solution containing 1.0 g of 2,2-bipyridine, 0.86 g of $FeCl_3{\cdot}6H_2O$, and 5 mL of deioned water, in which the molar ratio of 2,2-bipyridine to $FeCl_3{\cdot}6H_2O$ is 2:1. The resultant mixture was stirred as the solvent was evaporated at room temperature. The obtained powder was calcined at the given temperature for 3 h in high pure N_2, with a heating rate of 2 °C min^{-1}. The products were finally obtained by etching the silica templates in 20 wt % HF solution for 12 h. The prepared products were assigned as Fe−N−GC-*n* (*n* is the heat-treatment temperature). Other Fe−N−GC materials can be prepared by the same procedure using different nitrogen heterocyclic compounds such as *p*-aminotoluene, *p*-nitroaniline, and 2-amino pyridine.

Characterization. Powder X-ray diffraction patterns (XRD) were recorded on a Rigaku D/Max-2500 diffractometer (40 kV, 40 mA) with Cu Kα radiation. Transmission electron microscope (TEM) images were obtained on a JEM-2010 transmission electron microscope at an acceleration voltage of 200 kV. N_2 adsorption/desorption measurements were carried out at 77 K on a Micromeritics Tristar 3000 analyzer. X-ray photoelectron spectroscopy (XPS) measurements were performed on Axis Ultra DLD using Al Kα radiation, and C 1s (284.8 eV) was utilized as a reference to correct the binding energy. A Hitachi ST-4800 scanning electron microscope (SEM) was used to determine the morphology. The electrocatalytic activities of the as-prepared catalysts for ORR were evaluated by cyclic voltammetry (CV) and rotating disk electrode (RDE) techniques. A conventional three-electrode cell was employed incorporating a working glass carbon RDE (Pine, 5 mm), an Ag/AgCl, KCl (3 M) electrode as reference electrode, and a Pt electrode as counter electrode. The experiments in alkaline electrolytes were carried out in O_2-saturated 0.1 M KOH solution and the potential range is scanned between −1.2 and +0.2 V (vs Ag/AgCl) at a scan rate of 10 mV s^{-1} at the ambient temperature. The electrocatalytic activities for ORR in acidic electrolytes were investigated in O_2-saturated 0.1 M $HClO_4$ solution and the potential range is between 1.0 and −0.2 V (vs Ag/AgCl). The working electrodes in both cases were prepared through dispersing 10 mg of mesoporous NPMCs in 1.28 mL of an alcohol solution containing 30 μL of a 5 wt % Nafion solution by sonication. A commercially available 20 wt % Pt/C catalyst obtained from Johnson Matthey (JM) was used for comparison. Catalyst suspension was pipetted onto a polished glassy carbon electrode surface and then dried at room temperature. The general loading of active Fe−N−GC material on the working electrode is 0.2 mg cm^{-2} in 0.1 M KOH and 0.6 mg cm^{-2} in 0.1 M $HClO_4$ solutions. The catalyst loading of Pt/C on the electrode is 20 μg_{Pt} cm^{-2} in both cases. All the potentials are corrected to the RHE potentials according to the method reported in the literature[12] (see Figure S1). The ORR current is obtained by subtracting the current measured in N_2-saturated electrolyte from the current measured in O_2-saturated electrolyte. The onset ORR potential was defined as the electrode potential when ORR current density is 3 μA cm^{-2} in RDE polarization curves, according to the reported method in the literature.[13] The Koutecky−Levich (K−L) equations have been used to calculate the kinetic parameters:

$$\frac{1}{J} = \frac{1}{J_L} + \frac{1}{J_K} = \frac{1}{B\omega^{1/2}} + \frac{1}{J_K};\ B = 0.62nFC_0(D_0)^{2/3}\upsilon^{-1/6};\ J_K = nFkC_0$$

dx.doi.org/10.1021/cs401257j | ACS Catal. 2014, 4, 1793−1800

, in which J, J_K and J_L are the measured current density, kinetic- and diffusion-limiting current densities, respectively; ω is the angular velocity of the disk, n is the electrons transferred number in ORR, F is the Faraday constant (F = 96 485 C mol L^{-1}), C_0 is the bulk solubility of O_2, D_0 is diffusion coefficient of O_2, ν is thekinematic viscosity of the electrolyte, and k is the electron transfer rate constant. The number of electrons transferred (n) and J_K can be obtained from the slope and intercept of the K−L plots

RESULTS AND DISCUSSION

Structure, Morphology, and Component of Fe−N−GC. The ordered mesoporous structure of Fe−N−GC-900 material prepared by heating 2,2-bipyridine and iron salts at 900 °C was confirmed by the small-angle XRD pattern (Figure 2)

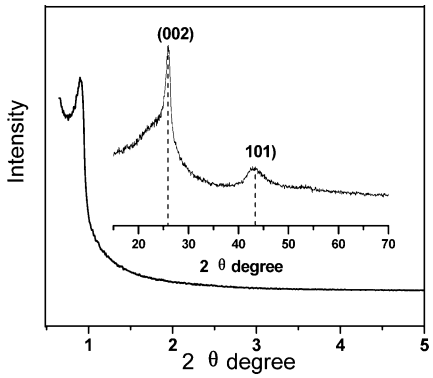

Figure 2. Small-angle and large-angle (inset) XRD patterns for Fe−N−GC-900.

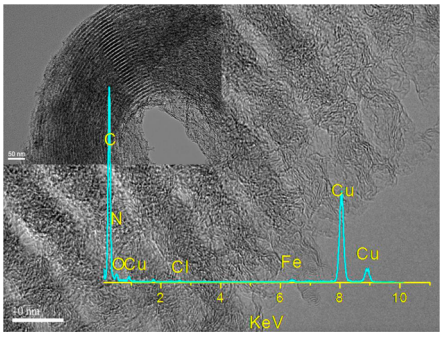

Figure 3. High-resolution TEM image of mesoporous Fe−N−GC-900. Inset images are the TEM image with a scale bar of 50 nm and TEM-EDS spectrum for Fe−N−GC-900.

and TEM images (Figure 3). There is a remarkable diffraction peak at about 2θ = 0.9° attributed to the (100) reflections of hexagonal mesostructures, which indicate that it is the inverted replica of SBA-15, similarly to CMK-3 mesoporous carbons. TEM images of Fe−N−GC-900 clearly display well-ordered nanoarrays and show that the mesopore is mainly from the slit-like pores between nanoarrays left over after the removal of SBA-15 silica templates. In the large-angle XRD pattern (Figure 2 inset), two remarkable peaks at 2θ = 26.5 and 43° ascribing to (002) and (101)[14] diffractions of graphitic carbons were observed. The corresponding selected-area electron diffraction (SAED) patterns for Fe−N−GC-900 (Figure S2) give the clear graphitic diffraction rings. The graphitic carbon stripes can be distinctly observed in the high-resolution TEM images (Figure 3). These facts sufficiently attest that Fe−N−GC-900 possesses a crystalline framework with high graphitization degree, which is profiting from the catalysis of Fe species for the decomposition and graphitization of the precursors.[15]

The mesoporoity and microporoity of Fe−N−GC-900 were investigated by N_2-adsorption and desorption techniques. A strong adsorption at lower relative pressure from 1 × 10^{-7} to 1 × 10^{-2} of P/P_0 indicates the existence of numerous micropores in the Fe−N−GC-900 (Figure 4). A remarkable H4 hysteresis

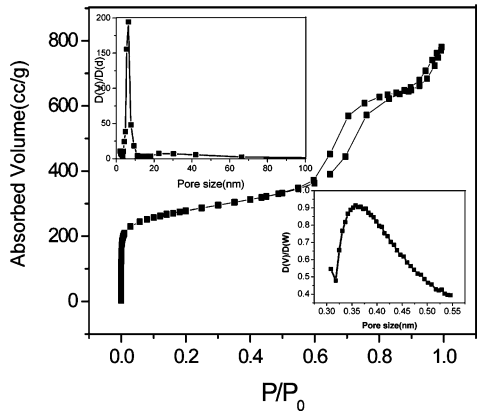

Figure 4. N_2-sorption isothermal and the corresponding pore size distribution curves (inset) for Fe−N−GC-900.

loop at the relative pressure range of 0.6−0.8 is a typical feature of N_2-adsorption and desorption isotherm for mesoporous materials. Fe−N−GC-900 has a higher BET surface area of 929 m^2 g^{-1}, which is composed of mesopore surface area of 499 m^2 g^{-1} and micropore surface area of 430 m^2 g^{-1} (Table S1), corresponding to their narrow mesopore size distribution centered at 6.3 nm and micropore size centered at 0.37 nm (Figure 4 inset). Such porous structure may facilitate the transportation and adsorption of O_2 in the Fe−N−GC-900 catalysts.

The TEM-EDS analysis (Figure 3 inset), SEM EDS-mapping results (Figure 5 and Figure S3), and XPS spectra (Figure 6) for Fe−N−GC-900 illustrate that this sample is composed of C, N, O, Cl, and Fe elements. The homogeneous distribution for Fe species observed in SEM EDS-mapping images (Figure 5B−D) gives an indication that Fe ions are doped in the carbon matrixes and there are not any bulk Fe-containing nanoparticles such as Fe, FeO_x, and FeC_x[16] in the prepared Fe−N−GC-900 material after the acid etching. The Fe 2p2/3 and N 1s XPS peaks have been fitted for further identifying the state of nitrogen and Fe species in the Fe−N−GC-900 materials (Figure 6 and Table S2). The N peaks at 398.3, 399.6, 401.0, and 403.eV in the deconvoluted N 1s XPS spectrum are known to originate from pyridinic (Py-N), pyrrolic (Pyr-N), graphitic-like (G-like), and oxidized type (Py-N−O) nitrogen, respectively. The pyridinic and pyrrolic nitrogen atoms can associate with Fe to form the catalytic active Fe−N_x sites.[17] A dominant peak centered at around 711 eV in the Fe 2p3/2 XPS spectrum should be ascribed to the N-coordinated Fe^{3+} or Fe^{2+}, and the other small fitting peak at about 716 eV may be the satellite peak of Fe ions or correspond to little of residual Fe−F species in the catalysts.[18] The XPS peak between 199.5 and 200.5 eV in the deconvoluted Cl 2p1/2 XPS spectrum for Fe−

dx.doi.org/10.1021/cs401257j | ACS Catal. 2014, 4, 1793−1800

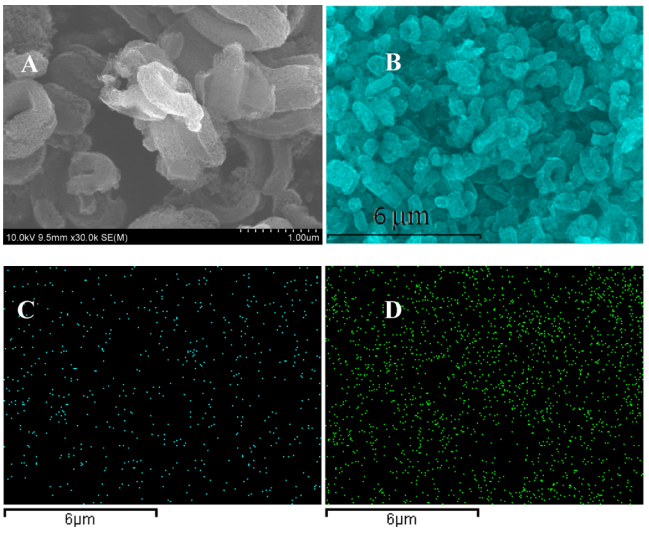

Figure 5. SEM image (A), the overall EDS-mapping images (B) for Fe, N, C, Cl, and O, and the individual Fe (C) and N (D) element mapping images for Fe−N−GC-900.

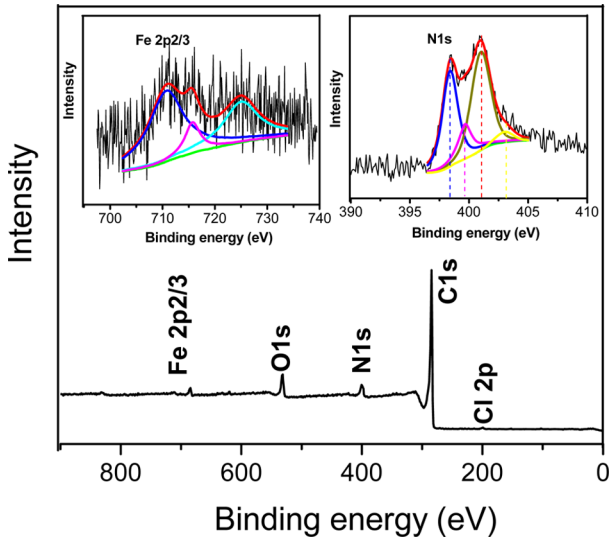

Figure 6. Full XPS spectrum for Fe−N−GC-900. Inset images are the deconvoluted N 1s and Fe 2p3/2 XPS spectra.

N−GC-900 may be ascribed to the Cl^- ions linked with Fe ions,[19] which may imply the existence of active Fe−N_x moieties in Fe−N−GC-900 material. All facts indicated that ordered hierarchically micro- and mesoporous graphitic architectures with active Fe−N_x moieties are successfully prepared by directly annealing the cost-effective 2,2-bipyridine and Fe^{3+} salts in confined SBA-15 mesochannels.

Electrocatalytic Activity for ORR. In order to comprehensively understand the catalytic performance of the prepared Fe−N−GC materials for ORR, the influence of the nitrogen heterocyclic precursors, heat-treatment temperature, and molar ratio of nitrogen source to iron salts in the preparation procedure on their catalytic activities was investigated in detail. The RDE polarization curves for ORR on the Fe−N−GC materials prepared by heating the mixtures comprising different molar ratio of 2,2-bipyridine to $FeCl_3{\cdot}6H_2O$ in 0.1 M KOH and 0.1 M $HClO_4$ solution (Figure S4) show that the optimized mole ratio of 2,2-dipyridine to iron salt in reaction mixtures is 2:1 among the investigated materials for the preparation of more active ORR electrocatalysts. Using different inexpensive nitrogen heterocyclic compounds such as *p*-aminotoluene, *p*-nitroaniline and 2-amino pyridine as the precursors, different ordered porous Fe−N−GC materials can be also obtained by heating the reaction mixtures comprising the 2:1 mol ratio of nitrogen heterocyclic compounds to iron salt. In terms of their ORR onset potential and E1/2 values determined by the polarization curves at 1600 rpm, it was concluded that the ORR activities of these Fe−N−GC materials prepared at the same temperature of 700 °C are remarkably different and increase from *p*-aminotoluene, *p*-nitroaniline, 2-amino pyridine to 2,2-dipyridine in both electrolytes (Figure 7A, Figure 8A, and Table S3, S4). This result may be attributed to the strong coordination effect between nitrogen and iron ions in the precursors which can facilitate the formation of more active Fe−N_x moieties and suitable textural structures. In this case, 2,2-dipyridine strongly chelating with iron ions become the best precursors for the synthesis of active Fe−N−GC catalysts. The polarization curves for ORR on the different Fe−N−GC materials prepared by heating the mixtures of 2,2-dipyridine and iron salts at different temperatures (600, 700, 800, 900, and 1000 °C) indicate that Fe−N−GC-900 prepared at 900 °C possess the best ORR activity in both 0.1 M KOH and 0.1 M $HClO_4$ solution (Figure 7B and Figure 8B; Tables S3 and S4). On the basis of the results above, it is believed that the Fe−N−GC-900 material prepared by heating the reaction mixtures comprising the 2:1 mol ratio of 2,2-bipyridine to $FeCl_3{\cdot}6H_2O$ at 900 °C possess the highest ORR activity in both electrolytes among these prepared Fe−N−GC materials, which should be the result from an appropriate combination between graphitization degree, textural structure, and active site density (see Figures 2−6; Figure S5; Tables S1−S4).

For the purpose of systematically exploring the catalytic behavior of the Fe−N−GC-900 material, its electrocatalytic properties for ORR were investigated in the N_2- or O_2-saturated solution by CV and RDE techniques. In the N_2-saturated 0.1 M KOH solution, the featureless voltammetric curves appeared for Fe−N−GC-900 materials, whereas in 0.1 M KOH electrolyte solution saturated with O_2, the prominent cathodic ORR peak at 0.87 V was observed, illustrating its effective ORR activity in alkaline medium (Figure 7C). The Fe−N−GC-900 electrode with 0.2 mg cm^{-2} loading display higher ORR onset potential (1.01 V) and half-wave potential (0.86 V) values determined by the polarization curves at 1600 rpm than over commercial Pt/C electrode with 20 μg_{Pt} cm^{-2} (Table S3), suggesting high intrinsic ORR activity and active site density of Fe−N−GC-900 in the O_2-saturated 0.1 M KOH solution. These values are even more positive than those obtained over the most promising NPMCs with 0.3−0.4 mg cm^{-2} catalyst loading in alkaline media.[12b,20] It is noticed that the ORR current density (J) over Fe−N−GC-900 measured at 1600 rpm are larger than those over Pt/C-JM at high potential regions (>0.7 V), and the calculated ORR kinetic-limiting current density over Fe−N−GC-900 (J_K, 9.6 mA cm^{-2}, Figure 7D) at 0.8 V is much higher than the J_k value over commercially available Pt/C-JM (5.2 mA cm^{-2}), indicating its high volumetric density of active sites and strong capability for mass- and charge-transport of Fe−N−GC-900 material.[14,21] These results indicate that the prepared Fe−N−GC-900 material is one of the best NPMCs in 0.1 M KOH alkaline medium.

The catalytic behavior of Fe−N−GC-900 in acidic medium has also been investigated. In contrast to the CV in N_2-

dx.doi.org/10.1021/cs401257j | ACS Catal. 2014, 4, 1793−1800

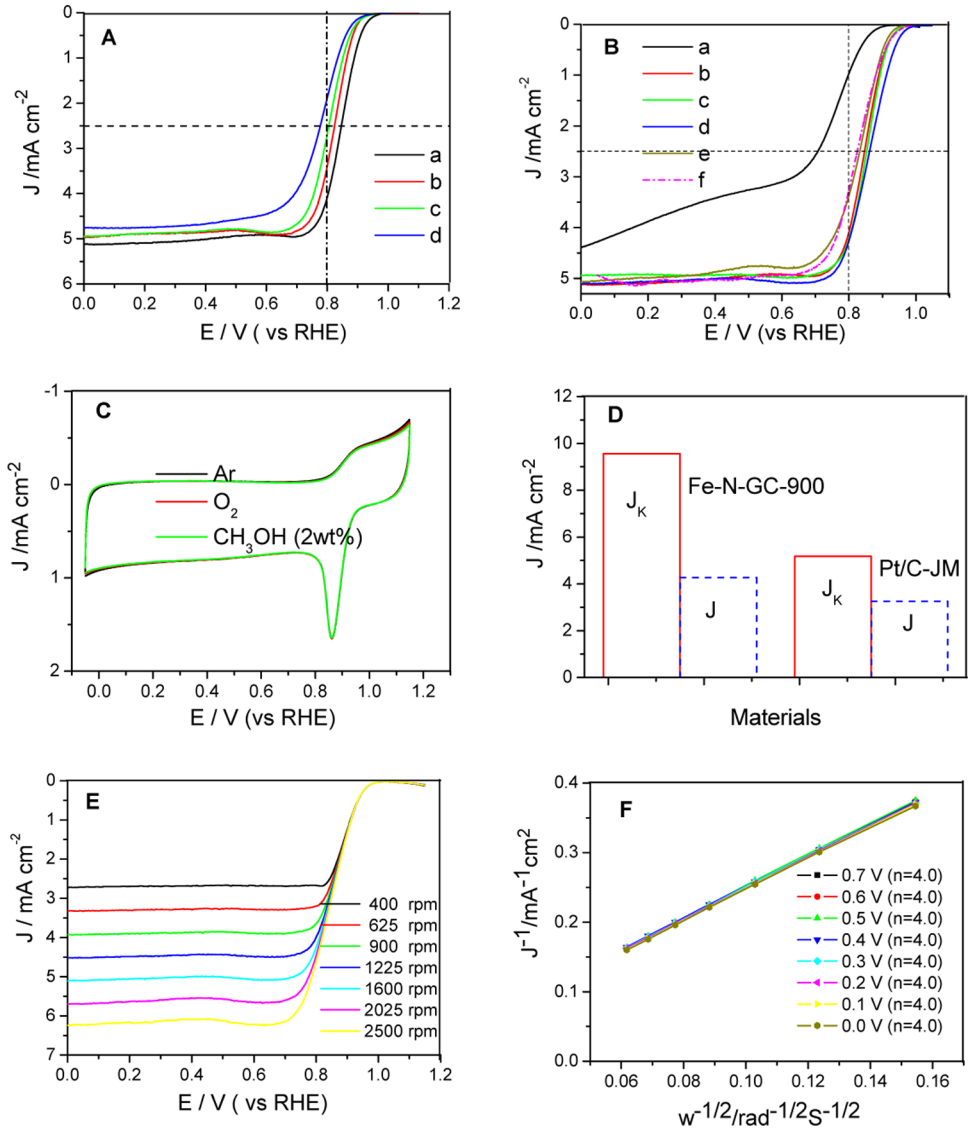

Figure 7. (A) RDE polarization curves of Fe−N−GC materials obtained by heating 2,2-bipyridine (a), 2-amino pyridine (b), *p*-nitroaniline (c), *p*-aminotoluene (d), and iron chloride at 700 °C; (B) RDE polarization curves recorded on Fe−N−GC materials prepared by heating 2,2-bipyridine and iron chloride at different temperatures (a, Fe−N−GC-600; b, Fe−N−GC-700; c, Fe−N−GC-800; d, Fe−N−GC-900; e, Fe−N−GC-1000) and Pt/C (f) materials at 1600 rpm; (C) CV curves on mesoporous Fe−N−GC-900 in 0.1 M KOH solution at a scan rate of 10 mV s^{-1}; (D) J and J_k current density for Fe−N−GC-900 at 0.8 V determined by the RDE polarization curves at 1600 rpm; (E) RDE polarization curves recorded for mesoporous Fe−N−GC-900 material at different rotation rates; (F). K−L plot of J^{-1} versus ω^{-1} on mesoporous Fe−N−GC-900 materials. The catalyst loadings on the electrodes are 0.2 mg cm^2 for Fe−N−GC materials and 20 μg_{Pt} cm^2 for Pt/C in 0.1 M KOH solution.

saturated 0.1 M $HClO_4$ solution (Figure 8C), an obvious ORR peak at 0.71 V is observed in O_2-saturated solution, revealing that Fe−N−GC-900 also has the efficient catalytic activity for ORR in acidic medium. The most optimized catalyst loading of Fe−N−GC-900 on the electrodes in acidic medium is 0.6 mg cm^{-2} according to the ORR polarization curves with different catalyst loadings at 1600 rpm, as shown in Figure S6. The E1/2 value (0.74 V) for ORR on the Fe−N−GC-900 electrode with 0.6 mg cm^{-2} loading is only slightly more negative than those obtained over Pt/C-JM with 20 μgPt cm^{-2} loading (0.78 V, Table S4) and the state-of-the-art reported NPMCs (PANI−Fe−Co−C).[6] The measured current density (5.2 mA cm^{-2}, 0.6 V) is higher than those over Pt/C-JM (4.6 mA cm^{-2}) and the PANI−Fe−Co−C (4.0 mA cm^{-2}),[6] which displays that the Fe−N−GC-4-900 has still a high catalytic performance for ORR in acidic medium.

ORR Kinential Process over Fe−N−GC-900. Because Fe−N−GC-900 material possesses excellent activity for ORR, the ORR kinetic process on it has also been investigated. The RDE polarization curves of ORR with an obvious platform in 0.1 M KOH solution saturated with O_2 can be seen in Figure 7E, which indicate that the ORR current on Fe−N−GC-900 catalysts becomes a completely mass-transfer-limited state in the potential range of 0.7 to 0 V. The corresponding K−L plots from the RDE polarization curves for Fe−N−GC-900 in Figure 7F between 0 and 0.7 V exhibited good parallel straight lines, similar to that over Pt/C catalyst (Figure S7), suggesting a reaction order of one with respect to oxygen and the same number of electrons transferred per oxygen molecule during the ORR in this potential range. According to the slope of the plots based on the K−L equations, the number of electrons transferred is calculated to be 4.0 at 0.5 V ($C_0 = 1.2 \times 10^{-3}$ mol

dx.doi.org/10.1021/cs401257j | ACS Catal. 2014, 4, 1793−1800

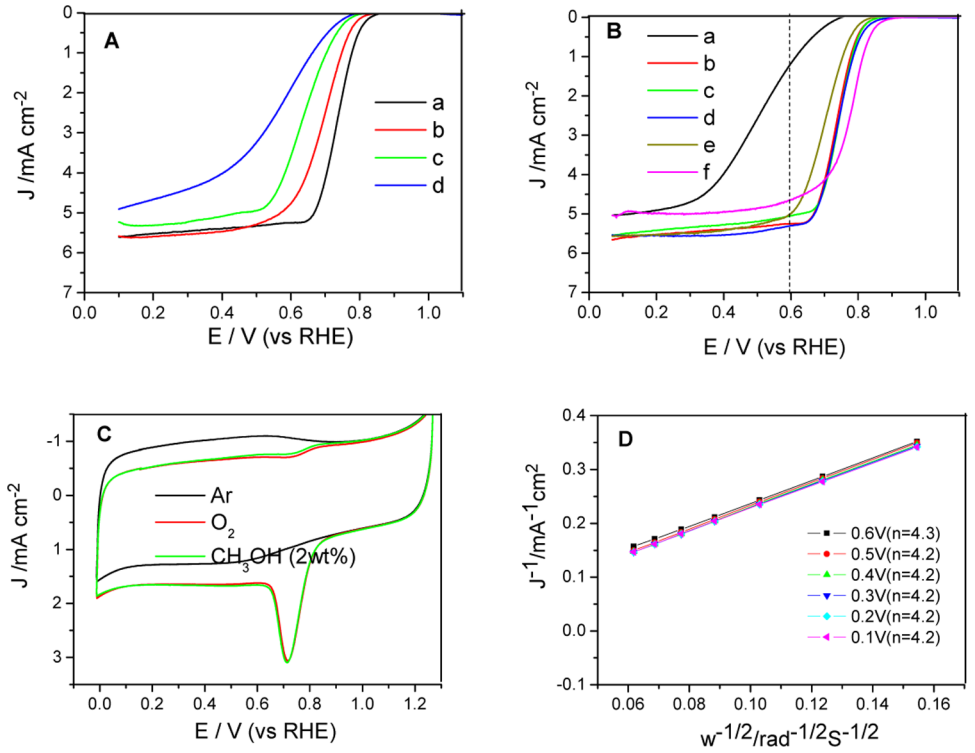

Figure 8. (A) RDE polarization curves of Fe−N−GC material by heating 2,2- bipyridine (a), 2-amino pyridine (b), *p*-nitroaniline (c), *p*-aminotoluene (d), and iron chloride at 700 °C in 0.1 M $HClO_4$ solution; (B) RDE polarization curves recorded on Fe−N−GC materials prepared by heating 2,2-bipyridine and iron chloride at different temperatures (a, Fe−N−GC-600; b, Fe−N−GC-700; c, Fe−N−GC-800; d, Fe−N−GC-900; and e, Fe−N−GC-1000) and Pt/C (f) materials at 1600 rpm; (C) CVs on mesoporous Fe−N−GC-900 in 0.1 M $HClO_4$ solution at a scan rate of 10 mV s^{-1}; (D) K−L plot of J^{-1} versus ω^{-1} on mesoporous Fe−N−GC-900 materials and Pt/C-JM at different potential. The catalyst loadings on the electrodes are 0.6 mg cm^2 for Fe−N−GC materials and 20 μg_{Pt} cm^2 for Pt/C in 0.1 M $HClO_4$ solution.

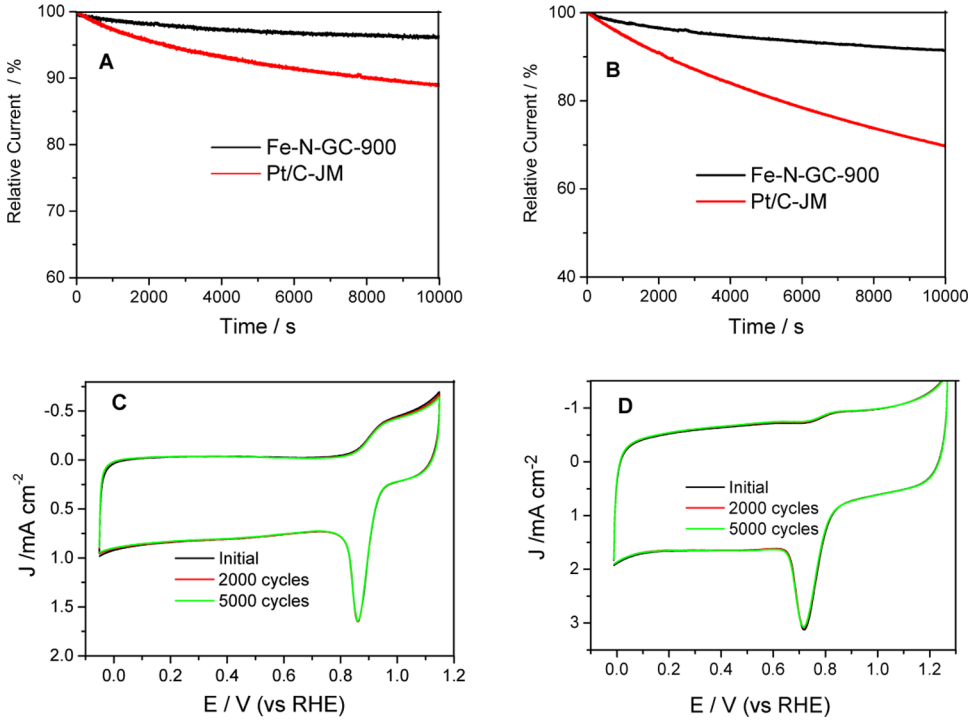

Figure 9. Current−time (I−T) chronoamperometric response of mesoporous Fe−N−GC-900 and Pt/C at 0.549 V in O_2-saturated 0.1 M KOH (A) and at 0.568 V in O_2-saturated 0.1 M $HClO_4$ (B) at a rotation rate of 1600 rpm; CV curves run for 5000 cycles recorded in O_2-saturated 0.1 M KOH (C) and 0.1 M $HClO_4$ (D) electrolytes for Fe−N−GC-900. The catalyst loading of mesoporous Fe−N−GC-900 on the electrodes is 0.2 mg cm^{-2} in 0.1 M KOH and 0.6 mg cm^{-2} in 0.1 M $HClO_4$ solution. The catalyst loading of Pt/C is 20 μg_{Pt} cm^{-2} in both media.

dx.doi.org/10.1021/cs401257j | *ACS Catal.* 2014, 4, 1793−1800

L^{-1}, $D_0 = 1.9 \times 10^{-5}$ cm s^{-1}, $\nu = 0.01$ cm^2 s^{-1}),[21b] meaning that Fe−N−GC-900 can catalyze a four-electron oxygen reduction reaction in 0.1 M KOH solution. A slightly sloping platform from 0.1 to 0.6 V was observed in the ORR polar curves of Fe−N−GC-900 in 0.1 M $HClO_4$ solution (Figure 8B,D), probably ascribing to a result of the highly porous nature of catalytic materials.[22] The corresponding K−L plots for Fe−N−GC-900 from 0.1 to 0.6 V also exhibited good linearity, and the corresponding electron transfer number is calculated to be 4.2 based on the K−L equations at 0.5 V ($C_0 = 1.13 \times 10^{-3}$ molL^{-1}, $D_0 = 1.9 \times 10^{-5}$ cm s^{-1}, $\nu = 8.93 \times 10^{-3}$ cm^2 s^{-1}).[23] These facts verify that Fe−N−GC-900 can efficiently reduce oxygen in a direct four-electron-reduction pathway with low overpotential in both alkaline and acidic media, thereby being stable enough under the respective conditions.

The electrocatalytic methanol-tolerant property and durability of Fe−N−GC-900 in both alkaline and acidic media were investigated. The significant impact of methanol on cathode peaks for ORR was observed in the CV curves on Pt/C-JM in O_2-saturated 0.1 M KOH and 0.1 M $HClO_4$ solution (Figure S8). However, no noticeable changes were found in the ORR peak potential and current over Fe−N−GC-900 in the absence or presence of methanol (2 wt %) (Figure 7A and 8A). The corresponding current−time (I−T) plots for Fe−N−GC-900 exhibited the relative slow attenuation (Figure 9). The relative current of 96% for ORR on Fe−N−GC-900 in 0.1 M KOH (Figure 9A) and 92% in 0.1 M $HClO_4$ solution (Figure 9B) still persisted after 10 000 s. In contrast, the ORR current on Pt/C-JM declined to approximately 88% in 0.1 M KOH and 70% in 0.1 M $HClO_4$ solution measured at the same conditions. Moreover, no obvious changes in the peak current and capacitive current for Fe−N−GC-900 were observed in the corresponding cyclic voltammograms for 5000 cycles recorded in O_2-saturated 0.1 M KOH (Figure 9C) and 0.1 M $HClO_4$ solution (Figure 9D), demonstrating a negligible degradation of surface active sites under the experimental conditions. It is observed that hierarchically porous graphitic Fe−N−GC-900 material affords the stable ORR active sites and restrains the degradation of active species in the ORR process.

CONCLUSIONS

In summary, this research work presents a simple method to obtain highly efficient ORR NPMCs by the direct construction of ordered hierarchically micro- and mesoporous Fe−N_x-embedded graphitic architectures. In the synthesis, the selection of nitrogen heterocyclic precursors, molar ratio of nitrogen source to iron salts, heat-treatment temperatures, and hard templates play the important roles in controlling the morphology of hierarchically porous Fe−N−GC materials, which strongly influences the active site density for ORR and the capability for O_2 transport in the prepared Fe−N−GC materials. The catalysis of Fe species for the decomposition and graphitization of the precursors results in the higher-graphitization-degree pore walls, which can give rise to the eminent electrob conductivity of the Fe−N−GC materials as electrocatalysts. The investigation results by CV and RDE polarization curves reveal that the ORR onset-potential, E1/2 value, and current density over the Fe−N−GC-900 electrode with 0.2 mg cm^{-2} loading are higher and larger than those obtained on commercial Pt/C-JM electrode with 20 μg_{Pt} cm^2 and the reported NPMCs with 0.3−0.4 mg cm^{-2} loading in 0.1 M KOH solution, which indicate that its catalytic activity is superior in alkaline medium. The ORR current density over the Fe−N−GC-900 electrode (0.6 mg cm^{-2} catalyst loading) measured at 0.6 V is larger than that on Pt/C-JM catalysts in 0.1 M $HClO_4$, exhibiting its efficient catalytic activity for ORR in acidic medium. Moreover, the Fe−N−GC-900 catalyst shows a direct four electron reduction pathway and durability toward ORR in both media as well as the excellent methanol-resistance. Ordered hierarchically micro- and mesoporous Fe−N_x−graphitic architectures prepared by this synthesis method using inexpensive nitrogen heterocyclic compounds and iron chlorides could be the practically promising nonprecious metal materials as cathode catalysts in PEMFCs.

ASSOCIATED CONTENT

Supporting Information

Structure, textural properties, and electrochemical measurement results for Fe−N−GC materials. This material is available free of charge via the Internet at http://pubs.acs.org/.

AUTHOR INFORMATION

Corresponding Author

*E-mail: ykshan@chem.ecnu.edu.cn.

Notes

The authors declare no competing financial interest.

ACKNOWLEDGMENTS

The authors are grateful to financial support from China National Natural Science Foundation (no. 21303058), Shanghai Municipal Natural Science Foundation (no. 13ZR1412400), and the key project of Shanghai Science and Technology Committee (no. 11JC1403400).

REFERENCES

(1) (a) Bezerra, C. W. B.; Zhang, L.; Lee, K.; Liu, H.; Marques, A. L. B.; Marques, E. P.; Wang, H.; Zhang, J. *Electrochim. Acta* **2008**, *53* (15), 4937−4951. (b) Brouzgou, A.; Song, S. Q.; Tsiakaras, P. *Appl. Catal., B* **2012**, *127*, 371−388. (c) Chen, Z.; Higgins, D.; Yu, A.; Zhang, L.; Zhang, J. *Energy Environ. Sci.* **2011**, *4* (9), 3167−3192. (d) Jaouen, F.; Proietti, E.; Lefevre, M.; Chenitz, R.; Dodelet, J.-P.; Wu, G.; Chung, H. T.; Johnston, C. M.; Zelenay, P. *Energy Environ. Sci.* **2011**, *4* (1), 114−130. (e) Wu, G.; Zelenay, P. *Acc. Chem. Res.* **2013**, *46* (8), 1878−1889.

(2) (a) Othman, R.; Dicks, A. L.; Zhu, Z. *Int. J. Hydrogen Energy* **2012**, *37* (1), 357−372. (b) Proietti, E.; Jaouen, F.; Lefèvre, M.; Larouche, N.; Tian, J.; Herranz, J.; Dodelet, J.-P. *Nat. Commun.* **2011**, *2*, 416.

(3) (a) Fu, X.; Liu, Y.; Cao, X.; Jin, J.; Liu, Q.; Zhang, J. *Appl.Catal., B* **2013**, *130*−*131*, 143−151. (b) Lefèvre, M.; Proietti, E.; Jaouen, F.; Dodelet, J.-P. *Science* **2009**, *324* (5923), 71−74.

(4) (a) Olson, T. S.; Chapman, K.; Atanassov, P. *J. Power Sources* **2008**, *183* (2), 557−563. (b) Liu, H.; Shi, Z.; Zhang, J.; Zhang, L.; Zhang, J. *J. Mater. Chem.* **2009**, *19* (4), 468−470.

(5) (a) Singh, D.; Soykal, I. I.; Tian, J.; von Deak, D.; King, J.; Miller, J. T.; Ozkan, U. S. *J. Catal.* **2013**, *304*, 100−111. (b) Morozan, A.; Jousselme, B.; Palacin, S. *Energy Environ. Sci.* **2011**, *4* (4), 1238−1254. (c) Serov, A.; Artyushkova, K.; Atanassov, P. *Adv. Energy Mater.* **2014**, 1301735.

(6) (a) Jaouen, F.; Dodelet, J.-P. *Electrochim. Acta* **2007**, *52* (19), 5975−5984. (b) Garsuch, A.; MacIntyre, K.; Michaud, X.; Stevens, D.; Dahn, J. *J. Electrochem. Soc.* **2008**, *155* (9), B953−B957.

(7) Bron, M.; Radnik, J.; Fieber-Erdmann, M.; Bogdanoff, P.; Fiechter, S. *J. Electroanal. Chem.* **2002**, *535* (1−2), 113−119.

(8) (a) Wu, G.; More, K. L.; Johnston, C. M.; Zelenay, P. *Science* **2011**, *332* (6028), 443−447. (b) Liu, S.-H.; Wu, J.-R. *Microporous Mesoporous Mater.* **2013**, *170*, 150−154.

(9) (a) Tian, J.; Birry, L.; Jaouen, F.; Dodelet, J.-P. *Electrochim. Acta* **2011**, *56* (9), 3276−3285. (b) Lefèvre, M.; Dodelet, J.-P. *Electrochim. Acta* **2008**, *53* (28), 8269−8276. (c) Jaouen, F.; Charreteur, F.; Dodelet, J.-P. *J. Electrochem. Soc.* **2006**, *153* (4), A689−A698.
(10) (a) Wood, T. E.; Tan, Z.; Schmoeckel, A. K.; O'Neill, D.; Atanasoski, R. *J. Power Sources* **2008**, *178* (2), 510−516. (b) Garsuch, A.; d'Eon, R.; Dahn, T.; Klepel, O.; Garsuch, R. R.; Dahn, J. R. *J. Electrochem. Soc.* **2008**, *155* (3), B236−B243.
(11) Chen, X.; Jun, Y.-S.; Takanabe, K.; Maeda, K.; Domen, K.; Fu, X.; Antonietti, M.; Wang, X. *Chem. Mater.* **2009**, *21* (18), 4093−4095.
(12) (a) Liang, Y.; Li, Y.; Wang, H.; Zhou, J.; Wang, J.; Regier, T.; Dai, H. *Nat. Mater.* **2011**, *10* (10), 780−786. (b) Cheon, J. Y.; Kim, T.; Choi, Y.; Jeong, H. Y.; Kim, M. G.; Sa, Y. J.; Kim, J.; Lee, Z.; Yang, T.-H.; Kwon, K.; Terasaki, O.; Park, G.-G.; Adzic, R. R.; Joo, S. H. *Sci. Rep.* **2013**, *3*, 2715.
(13) (a) Chokai, M.; Taniguchi, M.; Moriya, S.; Matsubayashi, K.; Shinoda, T.; Nabae, Y.; Kuroki, S.; Hayakawa, T.; Kakimoto, M.-a.; Ozaki, J.-i.; Miyata, S. *J. Power Sources* **2010**, *195* (18), 5947−5951. (b) Hu, Y.; Zhao, X.; Huang, Y.; Li, Q.; Bjerrum, N. J.; Liu, C.; Xing, W. *J. Power Sources* **2013**, *225*, 129−136.
(14) Liu, R.; von Malotki, C.; Arnold, L.; Koshino, N.; Higashimura, H.; Baumgarten, M.; Müllen, K. *J. Am. Chem. Soc.* **2011**, *133* (27), 10372−10375.
(15) Liang, C.; Li, Z.; Dai, S. *Angew. Chem., Int. Ed.* **2008**, *47* (20), 3696−3717.
(16) Wu, J.; Li, W.; Higgins, D.; Chen, Z. *J. Phys. Chem. C* **2011**, *115* (38), 18856−18862.
(17) Zhao, Y.; Watanabe, K.; Hashimoto, K. *J. Am. Chem. Soc.* **2012**, *134* (48), 19528−19531.
(18) Grosvenor, A. P.; Kobe, B. A.; Biesinger, M. C.; McIntyre, N. S. *Surf. Interface Anal.* **2004**, *36* (12), 1564−1574.
(19) Kim, Y. J.; Park, C. R. *Inorg. Chem.* **2002**, *41* (24), 6211−6216.
(20) (a) Chung, H. T.; Won, J. H.; Zelenay, P. *Nat. Commun.* **2013**, *4*, 1922. (b) Sun, X.; Song, P.; Zhang, Y.; Liu, C.; Xu, W.; Xing, W. *Sci. Rep.* **2013**, *3*, 2505.
(21) (a) Wen, Z.; Ci, S.; Zhang, F.; Feng, X.; Cui, S.; Mao, S.; Luo, S.; He, Z.; Chen, J. *Adv. Mater.* **2012**, *24* (11), 1399−1404. (b) Liu, R.; Wu, D.; Feng, X.; Müllen, K. *Angew. Chem.* **2010**, *122* (14), 2619−2623. (c) Zheng, Y.; Jiao, Y.; Chen, J.; Liu, J.; Liang, J.; Du, A.; Zhang, W.; Zhu, Z.; Smith, S. C.; Jaroniec, M.; Lu, G. Q.; Qiao, S. Z. *J. Am. Chem. Soc.* **2011**, *133* (50), 20116−20119. (d) Cong, H.-P.; Wang, P.; Gong, M.; Yu, S.-H. *Nano Energy* **2014**, *3*, 55−63.
(22) Ziegelbauer, J. M.; Olson, T. S.; Pylypenko, S.; Alamgir, F.; Jaye, C.; Atanassov, P.; Mukerjee, S. *J. Phys. Chem. C* **2008**, *112* (24), 8839−8849.
(23) Hu, Y.; Jensen, J. O.; Zhang, W.; Cleemann, L. N.; Xing, W.; Bjerrum, N. J.; Li, Q. *Angew. Chem., Int. Ed.* **2014**, *53* (14), 3675−3679.